Reductions in the thermal conductivity of irradiated silicon governed by displacement damage

Ethan A. Scott [1,2] Khalid Hattar [2] Eric J. Lang [2] Kiumars Aryana [1] John T. Gaskins [1,3] and Patrick E. Hopkins [1,4,5,*]
[1] *Department of Mechanical and Aerospace Engineering, University of Virginia, Charlottesville, Virginia 22904, USA*
[2] *Sandia National Laboratories, Albuquerque, New Mexico 87185, USA*
[3] *Laser Thermal Analysis, Inc., Charlottesville, Virginia 22902, USA*
[4] *Department of Materials Science and Engineering, University of Virginia, Charlottesville, Virginia 22904, USA*
[5] *Department of Physics, University of Virginia, Charlottesville, Virginia 22904, USA*

(Received 2 June 2021; revised 21 August 2021; accepted 15 September 2021; published 13 October 2021)

We report on the measured thermal conductivity of silicon irradiated with an array of ions: C^{2+}, N^{2+}, Al^{2+}, Si^{2+}, P^{2+}, and Ge^{2+}. Results are analyzed in consideration of ion mass, radius, and induced displacement damage. Recrystallization of select samples via annealing demonstrates that structural disorder imparted by incident ions, rather than the ions themselves, drive the reduction in thermal conductivity. This, in turn, is dictated by the mass of the ion. A generalized model is provided to relate thermal conductivity to displacement damage. Knowledge of the displacements-per-atom profile can thus be used to predict thermal conductivity reduction for silicon devices in extreme environments.

DOI: 10.1103/PhysRevB.104.134306

Materials in radiative environments (e.g., nuclear reactors, spacecraft, research instruments, among others) are subject to unique forms of damage. While studies on these materials often focus upon microstructure evolution or electronic properties [1–6], a fundamental understanding of their thermal properties is also of importance. For example, thermal conductivity decay in electronic devices or in materials used in reactors can lead to thermal failure [7]. Here we seek to experimentally demonstrate the influence of ion properties in the thermal conductivity decay of silicon, the most ubiquitous semiconductor material in electronic devices. Specifically, we assess the role of ion mass, radius, and fluence on irradiated silicon, and experimentally demonstrate a universality in the thermal conductivity reduction of ion irradiated solids based on displacements-per-atom (dpa) alone.

Several reports have utilized optical techniques to characterize the effect of ion irradiation on the thermal conductivity of crystalline silicon [7–12]. The majority of these works provide insight about modifications to thermal conductivity attributed to a given ion as a function of ion fluence or concentration. Long-established works on the scattering of phonons in defected crystals [13,14] assume that the scattering cross section of a defect is a function of the defect concentration as well as the relative difference in mass of the impurity and the localized strain that is induced. The change in strain is attributed to modifications to the atomic bonding environment due to the change in nearest neighbor distance that may occur from a difference in impurity radius [14].

These models work well to predict the change in thermal conductivity that occurs due to diffuse mass impurities introduced into a crystalline or alloyed system. However, additional complexities are introduced in the case where impurities are induced through ion irradiation. Incident ions are capable of leaving behind significant structural disorder along their trajectory [15], which degrades the crystallinity of the host lattice. While isolating independent phonon scattering mechanisms in irradiated materials can be a challenge, we devise an experiment which emphasizes the role of particular ion properties including the ion mass and radius. Here we report on the thermal conductivity of silicon implanted with ions of elements adjacent to silicon in the periodic table, which provides an array of masses and radii: C^{2+}, Al^{2+}, Si^{2+}, P^{2+}, and Ge^{2+}. Implantation with N^{2+} is performed as well for additional comparison. For each ion species, the thermal conductivity is measured as a function of fluence. The resultant trends are analyzed through modeling of the target damage. Furthermore, the role of implanted ions and the target damage induced by the ions are contrasted through an annealing and recrystallization study. Ultimately, a generalized model is produced to estimate thermal conductivity reduction of irradiated silicon as a function of the number of displacements induced by the implant, independent of the implant mass or radius.

Prior to sample implantation, stopping range of ions in matter (SRIM [16,17]) simulations were performed to determine implant depths and relative damage levels for an ion energy of 3.75 MeV [Figs. 1(a) and 1(b)]. For each ion, detailed calculations with full damage cascades were performed, which yield trends that correspond to the mass of the ion species. Lighter ions, such as C^{+} and N^{+} produce peak damage at deeper locations under the surface of the target. In contrast, heavier ions such as Ge^{+} produce a shallower implant, but a greater dpa due to the greater degree of nuclear stopping experienced by the heavier ions.

Following simulation, undoped single-crystal (100) silicon wafers were purchased from MTI Corporation and cleaved into samples approximately 5×5 mm^2 in area for use as the target material. The samples were adhered with carbon tape onto a silicon substrate, and loaded into an implant chamber pumped to vacuum on the order of 10^{-7} Torr. Implants were

*phopkins@virginia.edu

 ©2021 American Physical Society

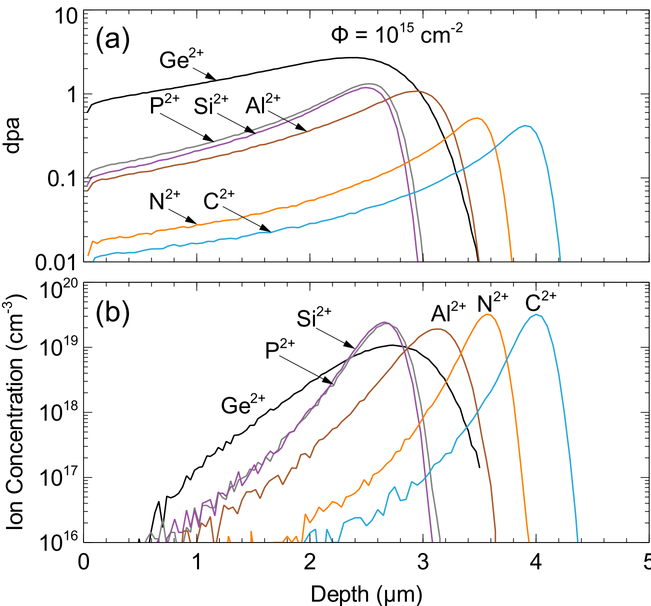

FIG. 1. SRIM simulations of the dpa profile (a) and ion concentration profile (b) for each ion implanted in a silicon target. The calculations assume a dose of 1×10^{15} cm^{-2}.

performed with a 6 MV tandem Van de Graaff accelerator. The ion beam, incident near-normal to the sample surface, was rastered to improve the spatial uniformity of the implant. Nominal fluences of 1×10^{13} to 1×10^{16} cm^{-2} were applied for each ion species.

Following the implantation, the samples were solvent cleaned followed by a 30 min O_2 plasma exposure to remove any carbon contamination induced during the implant procedure [9,18]. Samples were then coated with a nominally 80 nm film of aluminum, via electron beam evaporation, for use as an optothermal transducer for the time-domain thermoreflectance (TDTR) measurements of thermal conductivity [19].

Following irradiation, the structure of the silicon was analyzed via transmission electron microscopy (TEM) and selected area electron diffraction. A focused ion beam was used to prepare cross sections for all samples which were implanted at a nominal dose of 1×10^{15} cm^{-2}. In short, for all samples apart from the Ge^{2+} implant, crystallinity was maintained post-implant. The Ge^{2+} sample, however, showed no signs of crystalline diffraction over the depth of the implant, indicating that the irradiation from the heaviest ion induced amorphization within the implanted region for doses equal to or greater than 1×10^{15} cm^{-2}. Additional material regarding the TEM analysis is provided in the Supplemental Material [20].

The thermal conductivity of all samples was measured with TDTR. Nominal $1/e^2$ diameters of 17 and 10 μm were utilized for the focused pump and probe beams at powers of 26 and 5 mW, respectively. The measured ratio of the in-phase and out-of-phase signals from the lock-in detectors were subsequently analyzed with a multilayer heat diffusion model [21] for which thermophysical properties such as thermal conductivity can be treated as fit parameters. For the implanted samples, the $1/e$ thermal penetration depth (TPD) [22,23] was found to never exceed 1 μm. For all implanted samples, this does not approach the end of range. Furthermore, TEM analysis does not provide evidence of subsurface amorphous layer formation [24]. As such, the samples are modeled as a two-layer system consisting of an aluminum transistor atop a damaged substrate (additional details regarding the TDTR analysis are provided in the Supplemental Material [20]; see also Refs. [25,26] therein).

Among all ions, there are reductions in thermal conductivity as the fluence is increased in addition to general reductions corresponding to the mass of the implanted ion. For example, Ge^{2+} produces the highest degree of reduction compared to lighter ions such as Si^{2+} or C^{2+}. There is also an observable grouping trend among the samples that correspond to the atomic period of the implanted species. For example, C^{2+} and N^{2+}, ions from period II, display a similar thermal conductivity, as do period III ions, Al^{2+}, Si^{2+}, and P^{2+}.

Atomic displacements induced by implantation as well as the implanted ions themselves induce phonon scattering which reduces thermal conductivity. However, the relative contributions of scattering attributed to these sources can be difficult to separate when both forms of defects are present. Amorphous pockets and disordered regions in irradiated silicon have been shown to be stable at room temperature [27,28], but can diffuse and recrystallize at higher temperatures. Thus, annealing provides a means of emphasizing the role of mass-impurity scattering by recrystallizating the damaged lattice.

The mechanism of recrystallization in radiation-damaged silicon is solid phase epitaxial regrowth [29–31]. This requires the target to be sufficiently damaged or amorphized such that epitaxial regrowth will occur [32]. As the Ge^{2+}implanted samples demonstrate the highest degree of amorphization in addition to the highest concentration of ions in shallower depths [Fig. 1(b)], a second set of silicon samples were selected for an annealing study. The samples were irradiated in a similar manner as the original set, then annealed at high temperature to induce recrystallization. Details regarding the recrystallization of silicon and the anneal technique used here are provided in the Supplemental Material [20] (see also Refs. [33–37] therein).

The thermal conductivity of the second set of Ge^{2+} implants are shown in Fig. 2(b) for both the as-implanted and implanted/annealed state. The as-implanted samples trend in a similar manner to the Ge^{2+} implants in Fig. 2(a), with a thermal conductivity of less than 5 W m^{-1} K^{-1} at the highest dose. For the sample implanted at a dose of 1×10^{15} cm^{-2}, a higher thermal conductivity is measured, however, greater spatial variance was observed in the thermal conductivity, which could be attributed to nonuniformity in the implant area. Regardless, the thermal conductivity of all implanted samples are found to increase to that of the bulk thermal conductivity following anneal. The bulk-like thermal conductivity of the implanted/annealed samples demonstrates that the damage caused by the incident ions, rather than the implanted ions themselves, drive the reduction in thermal conductivity.

As implants were performed with a consistent ion energy and fluence, the distinguishing feature between the implants is the ion species. For each ion there will be a different ion mass and radius depending upon the atomic properties of the source element. We therefore consider the role of atomic mass

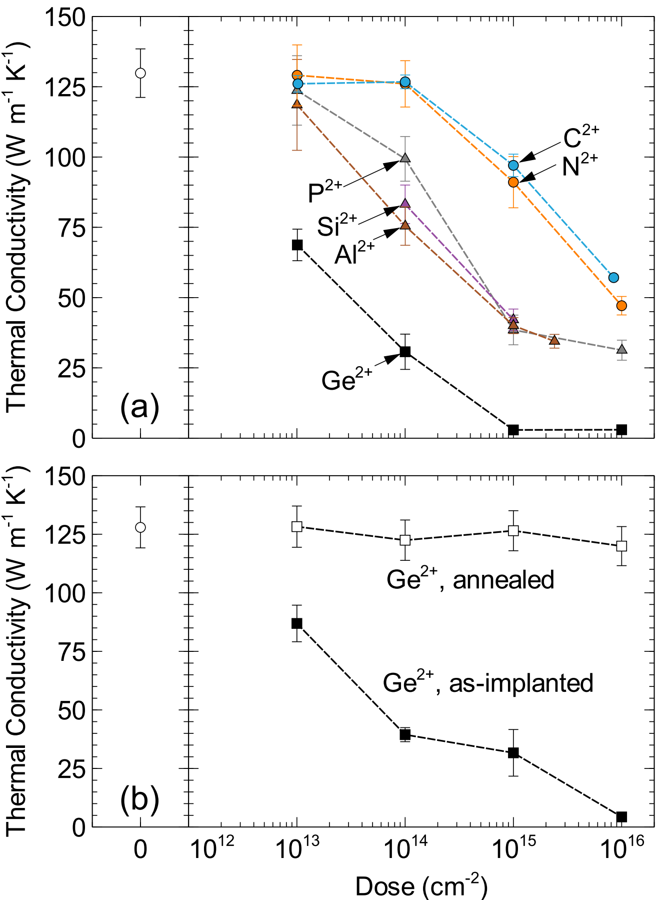

FIG. 2. Measured thermal conductivity as a function of ion dose for all as-implanted samples (a) as well as Ge^{2+} as-implanted/annealed (b).

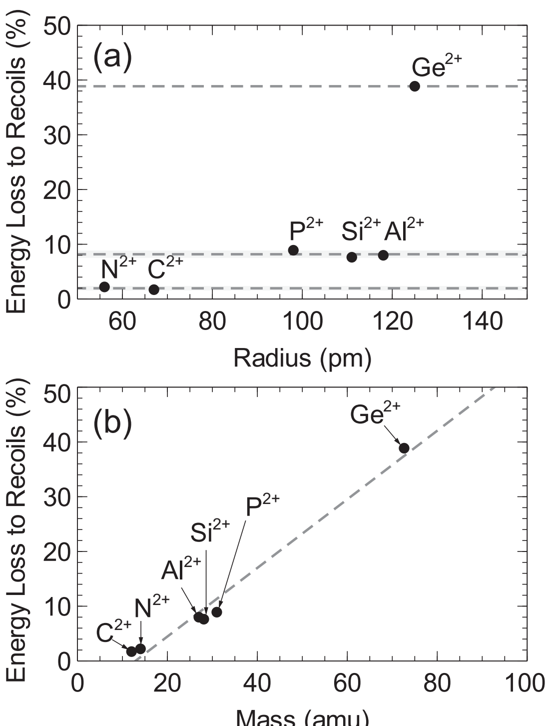

FIG. 3. Total energy loss to recoil events as a function of ion radius (a) and mass (b). The dashed line in (a) shows the average energy loss for a given atomic period, and in (b) is a linear fit to the data, which serves as a guide to the eye.

and radius upon the resultant silicon damage through SRIM modeling of the ion/target interaction. In short, there are two stopping mechanisms for an ion incident upon a target lattice: electronic and nuclear stopping [38]. In the initial phases of interaction, fast-moving ions are primarily slowed by electronic interactions with the target lattice [39,40], that is, the electrons of the host lattice reduce the energy and momentum of the incident ions. Electronic stopping often accounts for the bulk of ion energy dissipation, which produces an excitation of the host lattice electrons [39] and increases the temperature of the material [41]. Interaction of the ion and host lattice nuclei produces damage in the target via the formation of displacements. If the energy imparted to a lattice atom at rest is greater than the lattice binding energy, it will be dislodged from its equilibrium position yielding a displacement [38]. The recoiling atom can also dislodge other atoms at rest. This process will repeat to produce recoil cascades capable of vacancy formation in addition to amorphization of the material [12,42].

Thus, we consider the role of the atomic mass and radius in relation to nuclear energy loss mechanisms. The total energy loss to recoil events is calculated for each ion via SRIM simulation, shown in Fig. 3 as a function of atomic radius (a) and mass (b). The atomic radius for an ion implanted within a crystal is not well defined. However, for a qualitative analysis of the role of atomic radii, we consider the radii for each ion as calculated through minimal-basis-set self-consistent-field (SCF) functions [43].

Several trends emerge when the energy loss to recoils is plotted as a function of atomic radius [Fig. 3(a)]. There is a general increase in energy loss to recoils as the atomic radius increases; Ge^{2+} loses more energy to recoils than C^{2+}, for example. However, for the ions observed here, within a given atomic period, there is negligible correlation of atomic radii and energy loss to recoils. For example, P^{2+}, which has a radius 17% smaller than that of Al^{2+}, produces a nominally higher energy loss to recoils. Within a given atomic period, the energy loss to recoils is similar, displayed by the dashed lines in Fig. 3(a) of the average energy loss among ions in a given atomic period.

A stronger correlation in energy loss to recoils is observed as a function of ion mass, illustrated by the proportional relation Fig. 3(b). Successive increases in mass produce corresponding increases in energy loss to recoils. A linear fit between the parameters is shown in the figure, which serves as a guide to the eye. Taken together, the similarity in recoil energy loss for atoms of a given atomic period and the linear relation with ion mass demonstrates that ion mass plays a more influential role in producing displacement damage in the silicon target.

Increased energy loss to recoil cascades translates to higher dpa values. Thus, we consider the correlation between dpa and thermal conductivity. As shown in Fig. 1(a), the magnitude of the dpa is depth dependent. Here we consider the dpa within

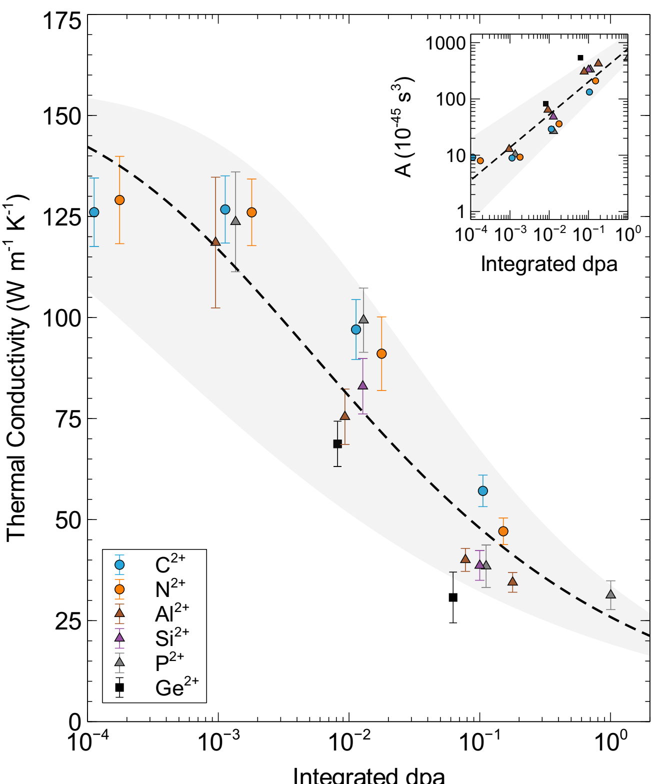

FIG. 4. Measured thermal conductivity of all ions as a function of integrated dpa. The dashed line models the data assuming a defect scattering coefficient proportional to the integrated dpa (shown in the inset). The gray region provides an upper and lower bound to the model accounting for a 95% confidence interval in the fitted relation between the scattering coefficient and the integrated dpa.

the depths spanning to the TPD. This range is calculated by solving the heat equation for a multilayered structure and determining the depth at which the temperature excursion falls to $1/e$ that of the surface [22,23]. The heater is assumed as a Gaussian source with a diameter equal to that of the effective spot size, modulated at the pump frequency of the TDTR measurements (8.8 MHz). Depending upon the thermal conductivity of the silicon and thermal boundary conductance (TBC), the TPD is found to range between 0.68 and 0.92 μm. As there is little sensitivity to the TBC of the high-dose Ge^{2+} implants, we do not model the TPD for those samples, however, it is expected to be below the minimum value of 0.68 μm.

The dpa sampled by the TDTR measurement is then considered as the total dpa integrated from the sample surface to the TPD. Depending upon the ion species and fluence, this yields values spanning 1.12×10^{-4} to 1 dpa. The thermal conductivity of all samples is plotted as a function of integrated dpa in Fig. 4. A consistent reduction in thermal conductivity is observed as a function of dpa. Because displacement damage is the dominant mechanism of thermal conductivity reduction, there is a similar trend among the data set in contrast to the dose-dependent thermal conductivity, which is also a function of ion mass.

To model the dpa-dependent trend, we consider the thermal conductivity from the framework of a Callaway-type model [44] (details provided in the Supplemental Material [20]). The thermal conductivity is subject to boundary, Umklapp, and defect scattering terms which are scaled by fitted coefficients. We assume the thermal conductivity reduction attributed to displacement damage to be represented by the defect scattering term $\tau_{\mathrm{defect}}^{-1} = A\omega^4$. For the boundary and Umklapp scattering rates, we utilize the forms and coefficients provided by Yang and Dames [45].

The magnitude of the defect scattering coefficient A can be obtained for each measured thermal conductivity value by interpolating the value of the measured thermal conductivity to the modeled thermal conductivity as a function of A (plotted in the Supplemental Material [20]). As we seek to model the thermal conductivity as a function of dpa, we correlate the calculated scattering coefficients with the integrated dpa values associated with each corresponding measured thermal conductivity. There is a proportional relationship between A and the integrated dpa, shown in the inset of Fig. 4. Given the approximately linear relation within log scaling, a power-law type relationship between the two parameters is assumed. With the fitted relation between A and the integrated dpa, the thermal conductivity is then calculated as a function of integrated dpa, shown as the dashed line in Fig. 4. The gray regions surrounding the model encompass the uncertainty attributed to a 95% confidence interval in the linear fit used to model A as a function of dpa. Despite the simplicity, this model provides a generalized tool to estimate the reduction in thermal conductivity of silicon in response to ion irradiation, which is independent of ion species and fluence.

In summary, single crystal silicon wafers were implanted with an array of ions of varying mass and radius, and the thermal conductivity was measured with TDTR. By recrystallizing select samples with high-temperature anneals, the reduction in thermal conductivity was attributed to the structural disorder induced by the incident ion rather than impurity scattering imparted by the ions themselves. Through analysis of the energy loss mechanisms, the mass of the ion was found to dictate the degree of target damage; ions of atoms within the same atomic period behave in a similar manner. Finally, the relation between radiation-induced damage and thermal conductivity was represented with a model in which the defect scattering rate is a function of the integrated dpa. Knowledge of particle energy and fluence could therefore be used to estimate potential thermal conductivity reduction for silicon devices in extreme environments.

The authors are grateful to Dr. Elbara Ziade for review of this manuscript. This work was supported, in part, by the Office of Naval Research, Grant No. 167236-101-GG12382-31345. This work was performed, in part, at the Center for Integrated Nanotechnologies, an Office of Science User Facility operated for the U.S. Department of Energy (DOE) Office of Science. Sandia National Laboratories is a multimission laboratory managed and operated by National Technology & Engineering Solutions of Sandia, LLC, a wholly owned subsidiary of Honeywell International, Inc., for the U.S. DOE's National Nuclear Security Administration under Contract No. DE-NA-0003525. The views expressed in the article do not necessarily represent the views of the U.S. DOE or the United States Government.

[1] B. Li, H. Liu, T. Shen, L. Xu, J. Wang, F. Zhao, D. Peng, J. Li, Y. Sheng, and A. Xiong, J. Eur. Ceram. Soc. **40**, 1014 (2020).
[2] X. Li, Y. Jia, X. Zhou, Y. Zhao, Y. Tang, Y. Li, G. Liu, and G. Jia, IEEE Electron Device Lett. **41**, 216 (2019).
[3] J. G. Gigax, E. Aydogan, T. Chen, D. Chen, L. Shao, Y. Wu, W. Y. Lo, Y. Yang, and F. A. Garner, J. Nucl. Mater. **465**, 343 (2015).
[4] C. Abbate, G. Busatto, P. Cova, N. Delmonte, F. Giuliani, F. Iannuzzo, A. Sanseverino, and F. Velardi, IEEE Trans. Nucl. Sci. **62**, 202 (2015).
[5] G. Soelkner, Microelectron. Reliab. **58**, 39 (2016).
[6] J. A. Felix, M. R. Shaneyfelt, J. R. Schwank, S. M. Dalton, P. E. Dodd, and J. B. Witcher, IEEE Trans. Nucl. Sci. **54**, 2181 (2007).
[7] R. Cheaito, C. S. Gorham, A. Misra, K. Hattar, and P. E. Hopkins, J. Mater. Res. **30**, 1403 (2015).
[8] M. Khafizov, C. Yablinsky, T. R. Allen, and D. H. Hurley, Nucl. Instrum. Methods Phys. Res., Sect. B **325**, 11 (2014).
[9] C. S. Gorham, K. Hattar, R. Cheaito, J. C. Duda, J. T. Gaskins, T. E. Beechem, J. F. Ihlefeld, L. B. Biedermann, E. S. Piekos, D. L. Medlin, and P. E. Hopkins, Phys. Rev. B **90**, 024301 (2014).
[10] E. A. Scott, K. Hattar, C. M. Rost, J. T. Gaskins, M. Fazli, C. Ganski, C. Li, T. Bai, Y. Wang, K. Esfarjani, M. Goorsky, and P. E. Hopkins, Phys. Rev. Mater. **2**, 095001 (2018).
[11] S. Alaie, M. G. Baboly, Y.-B. Jiang, S. Rempe, D. H. Anjum, S. Chaieb, B. F. Donovan, A. Giri, C. J. Szwejkowski, J. T. Gaskins, M. M. M. Elahi, D. F. Goettler, J. Braun, P. E. Hopkins, and Z. C. Leseman, ACS Appl. Mater. Interfaces **10**, 37679 (2018).
[12] H. S. Choe, R. Prabhakar, G. Wehmeyer, F. I. Allen, W. Lee, L. Jin, Y. Li, P. Yang, C.-W. Qiu, C. Dames, M. Scott, A. Minor, J.-H. Bahk, and J. Wu, Nano Lett. **19**, 3830 (2019).
[13] P. G. Klemens, Proc. Phys. Soc. A **68**, 1113 (1955).
[14] B. Abeles, Phys. Rev. **131**, 1906 (1963).
[15] A. Abdullaev, V. S. Chauhan, B. Muminov, J. O'Connell, V. A. Skuratov, M. Khafizov, and Z. N. Utegulov, J. Appl. Phys. **127**, 035108 (2020).
[16] J. F. Ziegler, M. D. Ziegler, and J. P. Biersack, Nucl. Instrum. Methods Phys. Res. Sect. B **268**, 1818 (2010).
[17] J. F. Ziegler, Nucl. Instrum. Methods Phys. Res. Sect. B **219**, 1027 (2004).
[18] P. E. Hopkins, K. Hattar, T. Beechem, J. F. Ihlefeld, D. L. Medlin, and E. S. Piekos, Appl. Phys. Lett. **98**, 231901 (2011).
[19] P. Jiang, X. Qian, and R. Yang, J. Appl. Phys. **124**, 161103 (2018).
[20] See Supplemental Material at http://link.aps.org/supplemental/10.1103/PhysRevB.104.134306 for additional details regarding TEM, sample annealing, and thermal measurements and analysis.
[21] D. G. Cahill, Rev. Sci. Instrum. **75**, 5119 (2004).
[22] J. L. Braun and P. E. Hopkins, J. Appl. Phys. **121**, 175107 (2017).
[23] J. L. Braun, C. J. Szwejkowski, A. Giri, and P. E. Hopkins, J. Heat Transfer **140**, 052801 (2018).
[24] E. A. Scott, J. L. Braun, K. Hattar, J. D. Sugar, J. T. Gaskins, M. Goorsky, S. W. King, and P. E. Hopkins, J. Appl. Phys. **129**, 055307 (2021).
[25] D. H. Olson, J. A. Deijkers, K. Quiambao-Tomko, J. T. Gaskins, B. T. Richards, E. J. Opila, P. E. Hopkins, and H. N. G. Wadley, Mater. Today Phys. **17**, 100304 (2021).
[26] P. Flubacher, A. J. Leadbetter, and J. A. Morrison, Philos. Mag. **4**, 273 (1959).
[27] K. Nordlund, S. J. Zinkle, A. E. Sand, F. Granberg, R. S. Averback, R. E. Stoller, T. Suzudo, L. Malerba, F. Banhart, W. J. Weber, F. Willaime, S. L. Dudarev, and D. Simeone, J. Nucl. Mater. **512**, 450 (2018).
[28] H. Hensel and H. M. Urbassek, Phys. Rev. B **57**, 4756 (1998).
[29] J. S. Williams, Nucl. Instrum. Methods Phys. Res. **209**, 219 (1983).
[30] F. Corni, S. Frabboni, G. Ottaviani, G. Queirolo, D. Bisero, C. Bresolin, R. Fabbri, and M. Servidori, J. Appl. Phys. **71**, 2644 (1992).
[31] R. Duffy, T. Dao, Y. Tamminga, K. van der Tak, F. Roozeboom, and E. Augendre, Appl. Phys. Lett. **89**, 071915 (2006).
[32] T. L. Alford, D. C. Thompson, J. W. Mayer, and N. D. Theodore, J. Appl. Phys. **106**, 114902 (2009).
[33] H. Kruutle, Radiat. Eff. **24**, 255 (1975).
[34] L. Sealy, R. C. Barklie, W. L. Brown, and D. C. Jacobson, Nucl. Instrum. Methods Phys. Res. Sect. B **80**, 528 (1993).
[35] J. W. Mayer, L. Eriksson, S. T. Picraux, and J. A. Davies, Can. J. Phys. **46**, 663 (1968).
[36] D. N. Lee and S. B. Lee, *Advanced Topics in Crystallization* (IntechOpen, 2015).
[37] L. Pelaz, L. A. Marques, and J. Barbolla, J. Appl. Phys. **96**, 5947 (2004).
[38] J. F. Ziegler, *The Stopping and Ranges of Ions in Matter: Handbook of Stopping Cross-Sections for Energetic Ions in All Elements* (Elsevier, Amsterdam, 2013), Vol. 5.
[39] A. Schleife, Y. Kanai, and A. A. Correa, Phys. Rev. B **91**, 014306 (2015).
[40] C. P. Race, D. R. Mason, M. W. Finnis, W. M. C. Foulkes, A. P. Horsfield, and A. P. Sutton, Rep. Prog. Phys. **73**, 116501 (2010).
[41] D. M. Duffy and A. M. Rutherford, J. Phys.: Condens. Matter **19**, 016207 (2006).
[42] P. Leveque, H. K. Nielsen, P. Pellegrino, A. Halln, B. G. Svensson, A. Yu. Kuznetsov, J. Wong-Leung, C. Jagadish, and V. Privitera, J. Appl. Phys. **93**, 871 (2003).
[43] E. Clementi, D. L. Raimondi, and W. P. Reinhardt, J. Chem. Phys. **47**, 1300 (1967).
[44] J. Callaway, Phys. Rev. **113**, 1046 (1959).
[45] F. Yang and C. Dames, Phys. Rev. B **87**, 035437 (2013).